Advanced Functional Materials

ADVANCED FUNCTIONAL MATERIALS
www.afm-journal.de

RESEARCH ARTICLE OPEN ACCESS

Shaping of Biohybrid Functional Living Materials

Sarah Schyck | Mark Ablonczy | Sourav Patranabish | Kunal Masania

Shaping Matter Lab, Faculty of Aerospace Engineering, Delft University of Technology, Delft, Netherlands

Correspondence: Kunal Masania (k.masania@tudelft.nl)

Received: 15 November 2025 | **Revised:** 2 March 2026 | **Accepted:** 11 March 2026

Keywords: additive manufacturing | biohybrid materials | engineered living materials | mycelium composites

ABSTRACT

As society seeks alternatives to energy-intensive manufacturing, biological growth offers an underexplored route for material fabrication. While prior studies have demonstrated direct ink writing of mycelium-based composites, these approaches often use mycelium only as a structural filler. Here, we exploit active hyphal growth as a post-printing, growth-driven functionalization mechanism to self-assemble particles and tune material properties. When micro- and nano-particles are introduced into the liquid growth medium, their incorporation follows distinct, size-dependent pathways. Nanoparticles adsorb onto and armor the hyphae, whilst micron-sized particles become physically entangled within the growing network. By printing inoculated, cross-linkable hydrogels via direct ink writing, we spatially confine the mycelial architecture without disrupting growth. We introduce selective particle deposition using a dissolvable gelatin mask, enabling localized functionalization. We explore how the shape morphology evolves as the mycelium grows from the hydrogel scaffold into the media. Incorporation of conductive carbon particles enhances the native bioelectric signaling, increasing the signal-to-noise ratio by 2.7-fold and peak amplitude by 9-fold. Together, these findings establish a growth-programmable living fabricating strategy, where multifunctional materials can self-assemble through the natural expansion of living networks.

1 | Introduction

Fungi, particularly filamentous species, play a crucial role in the development of sustainable biogenic materials, which are materials produced by living organisms. Their fibrous, biodegradable networks can replace traditional synthetic materials, providing renewable routes to materials for structural [1, 2], packaging [3], and even biomedical [4] applications. The functionality of these materials can be remarkably enhanced when the organism is kept alive, for example, by leveraging self-healing, adaptiveness, morphogenesis, and even communication via bioelectric signaling within the living material [5]. This can be further enhanced through emerging tools in 3D printing, advanced manufacturing, and genetic engineering, which allow us to shape, functionalize, and program living fungal systems with unprecedented precision.

Despite significant progress in using mycelium as a functional material, there remains a need for approaches that more directly couple fungal biology with engineered control over material properties. In particular, strategies that integrate mycelium growth, functionality, and precise shaping could produce multifunctional, structurally defined biohybrid materials. We propose that if this natural growth process could be harnessed, it would be possible to assemble reactive or functional particles into the mycelium network. This would transform the mycelium into building blocks for biohybrid engineered living materials capable of sensing, remediation, or energy transduction.

Achieving this requires strategies that bridge the gap between biology and engineering. The first begins with the fungus itself, its remarkable ability to sense and respond to its environment, altering both its morphology and composition in response to

external stimuli [6]. Advances in fungal genetics have enabled precise tuning of the intrinsic properties of mycelium-based materials [7]. Adjusting nutrient composition yields denser mycelium networks [8] while controlling culture parameters, such as agitation, modulates pellet morphology for *Aspergillus niger*, enhancing its protein production [9]. Mycelium can also function as a biological fiber factory, producing biopolymeric fibers with tunable mechanical properties [10]. Mycelium's functionality further extends to electronics and sensing. Fungal networks can mediate redox reactions as electron-transfer agents in microbial fuel cells [11], and genetically engineered mycelium has been programmed as color-changing biosensors that detect xylose [12], offering an effective natural monitoring platform.

Building on these intrinsic biological properties, mycelium functionality can be further extended by integrating nano- and micro-materials directly into the fungal network to create responsive, multifunctional materials. Such hybridization enables control over electrical, chemical, and other properties at multiple scales. Mycelium-carbon nanotube (CNT)-polyvinyl alcohol (PVA) [13] or mycelium-polyacrylamide (PAM)-polyaniline (PANI) [14] composites, for example, exhibit regenerative capabilities while serving as sensors or electrodes. Biocomposites prepared from hyphae embedded with nanocellulose show improved wet resistance and mechanical strength [15]. Mycelium pellets are adept at integrating additive materials, as they are capable of collecting twice their own weight in microplastics [16] and integrating several nano- and micro-material types [17]. On the other hand, fungal mycelium can nucleate various kinds of particles due to its rich microenvironment [18–22] that can then be self-assembled along the hyphae to create functional, fungal-templated structures [23–28].

More recent work combines fungal growth with additive manufacturing to create designed living composites. For example, 3D printing of the basidiomycete *Fomes fomentarius* in alginate-rapeseed straw hydrogels produced ultralightweight structures [29] while pressed composites exhibited mechanical and thermal properties comparable to those of conventional insulation materials [30]. Similarly, *Ganoderma lucidum* composites grown in 3D-printed molds utilize agro-industrial waste to form sound-absorbing panels [31], while *Aureobasidium pullulans* has been processed, into a protective stain-like coating for wood surfaces [32]. This growing interest in living construction materials reflects the transition toward sustainable, low-carbon construction [33, 34], including hybrid wood-fungi composites that exhibit enhanced tensile strength [35]. Furthermore, direct ink writing of mycelium allows the creation of shapeable, self-repairing, and adaptive living structures [36], often in combination with agro-industrial waste such as spent coffee grounds [37, 38]. At larger scales, mycelium composites have also been shaped through wire-cutting techniques to enable industrial production [39].

While recent systems have demonstrated the potential of fungi in material fabrication, they often remain limited in their ability to precisely control the 3D spatial structure of mycelium, integrate functional materials into the matrix, and customize local material properties within a hybrid material. As a result, fungi are frequently employed as passive structural matrices rather than as responsive, actively assembling components. To address these challenges, we propose a strategy that combines biological self-assembly with engineered shaping to enable selective material deposition and hierarchical patterning of fungal biohybrids. By modernising and adapting widely used industrial liquid fermentation methods, we aim to establish a scalable, cost-effective route to produce hybrid engineered living materials (ELMs) with programmable structure and function.

However, developing a functional fungal engineered living material requires understanding how the organism grows, interacts with its environment, and how this growth can be guided into a designed form. In our work, we look to bridge natural and engineered routes to functional fungal materials by integrating nano- and micro-particles with desirable properties in a mycelium network growing from a defined shape. When fungi are cultured in a liquid medium under agitation, mycelium forms tightly packed pellets, as depicted in Figure 1a. In contrast, in natural environments, mycelia interact with a heterogeneous microenvironment. They adsorb and internalize nanoparticulate colloidal nutrients for themselves or their host, sometimes via endocytosis-like processes, and can be as large as ~200 nm [40], through surface binding, enzymatic or small molecule solubilization, or endocytosis-like processes. Therefore, when nano- or micro-particles are added to the fermentation media, mycelium pellets are likely to adsorb particles within the mycelial network or directly along the hyphal cell wall [13, 15, 17, 25, 41] schematically shown in Figure 1b (i). Depending on the type of adsorbed particle, we can create mycelium pellets that are inherently functionalized. Alongside this, recent advances have explored the use of mycelium-laden hydrogels as structured scaffolds, providing defined anchoring points for fungal growth [36]. We can modify these hydrogels to withstand submerged fermentation conditions, enabling the growth and functionalization of mycelium biohybrid materials that retain their biological activity and designed structure, shown schematically in Figure 1b (ii). In this work, we utilize these techniques to develop a functional biohybrid material that enhances and augments the natural bioactivity of the fungi themselves (Figure 1c). This approach may yield a living material that combines biological self-organization with engineered form and functionalization.

2 | Results and Discussion

To understand how mycelium-based materials can be engineered across scales, we examine how particles are incorporated into the growing mycelial network, how structural shaping through 3D printing influences their distribution, and how these factors affect the resulting functional response, following the transition from natural pellet formation to controlled, spatially functionalized, fungal materials.

2.1 | Fungal Pellet Formation and Growth

To explore how mycelium pellets develop during the growth phase, we prepare malt extract broth (MEB), which provides the mycelium with the nutrients needed for sustained growth. We inoculate the MEB with active hyphal tips to seed the initial pellets. The cultures are then incubated at a controlled temperature and under agitation for seven days, allowing the pellets to grow and mature while maintaining consistent conditions. During this

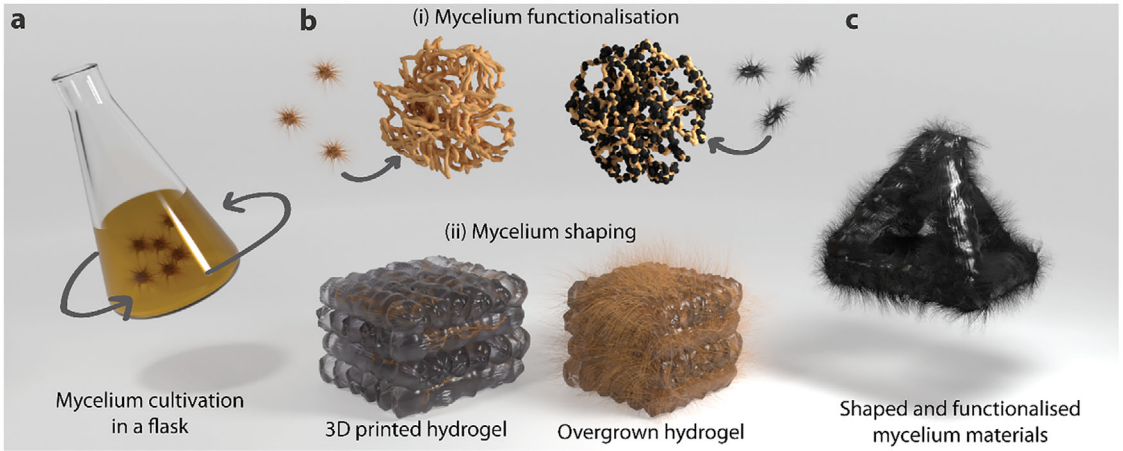

FIGURE 1 | Schematic overview of the growth, functionalization & shaping we perform to form functional biohybrid living materials. (a) Mycelium cultivated in a shaking flask forms into pellets, with morphologies dependent on shaking rate, nutrient concentration, and incubation time. (b) Mycelium cultivated in a medium with nano- and micro-particles (i) adsorbs suspended particles into the mycelium network, forming functional pellets. (ii) Active mycelium fragments embedded into a 3D-printable bioink grow into specific, architected designs. (c) By combining these techniques, biohybrid engineered living materials can have specific functionalization along an architected feature that could, for instance, enhance the bio-electrical interface between the materials and electrodes.

incubation period, pellets undergo morphological changes that reflect their growth conditions.

In general, mycelium pellets undergo radial growth in agitated liquid media, as shown in Figure 2a, which displays the pellets on days three and seven of growth. This growth can be divided into three distinct rings, schematically shown in Figure 2b, characterized by differing hyphal activity and susceptibility to fragmentation. The outer shell consists of relatively loose hyphae that appear "hairy" and can fragment due to shear forces, reseeding into secondary pellets. The active middle shell contains metabolically active hyphae with access to dissolved oxygen and nutrients, whereas the inner starvation core is nutrient- and oxygen-depleted, leading to autolysis. Growth of the pellet is strongly influenced by the balance between hyphal extension at the surface and the loss of material via fragmentation and autolysis [9].

Pellet formation begins at active hyphal tips or spawn sites, where new hyphae grow and branch from to form the initial mycelial network. Figure S1 shows fluorescent microscopy over the first 16 h of mycelium growth. As the newly formed pellets grow, they can entangle with nearby ones, creating connections that quickly increase the size of the pellets on the macroscale (Figure S2). Pellet growth is often modeled as a shell structure, where hyphal extension occurs primarily at the surface [42–44]. In such models, the pellet radius, R_p, and its expansion rate, $\frac{dR_p}{dt}$, are governed by surface growth rate outside the starvation core, which becomes limited when the core grows. Fragmentation, driven by shear stress from agitation, is the other main factor that controls the pellet size [45, 46]. When shear stress exceeds the strength of the hyphal wall, the pellets fragment the hyphae at the surface, seeding the formation of secondary pellets. As the inactive core grows, autolysis can lead to increased vacuolation, which helps maintain the turgor pressure required for hyphal extension at their tips, resulting in higher fragmentation as the mycelium ages [44, 47, 48]. However, this also weakens the pellet structure, making it more susceptible to fragmentation and further formation of new secondary pellets.

Pellet size in liquid culture is therefore closely linked to fluid shear, which scales with the Reynolds' number. Lower agitation produces singular, large pellets, while higher agitation yields smaller and more fragmented pellets, shown in the optical image insets in Figure 2b. Under standard conditions, pellet growth followed a first-order model [42] of the form $\frac{dR_p}{dt} = K - \beta R_p$ where K is the radial growth rate and β is the fragmentation coefficient, resulting in a K/β of 0.57. This means that the overall shear forces limit the growth of the pellet, resulting in slowed diameter growth after seven days. Therefore, by increasing this ratio via the reduction of the agitation rate, we can predict and control the evolution of the pellets during fermentation. We explore this by measuring pellet radii for 10+ pellets over three batches of mycelium cultivated in a 250 mL Erlenmeyer flasks shaking at 160 rpm as shown in Figure 2c. The first two days of growth, the mycelium form small pellets without a strong spherical shape (Figure S2) and the difference between repetitions can reach 0.1-0.2 cm for a global mean of 0.06 cm and 0.12 cm, for the first and second day respectively. Over the next five days, the repetition average narrows to a difference of 0.16 cm for a global mean of 0.44 cm.

To explore how particles adsorb and interact with mycelium pellets during growth, we selected carbon-based particles of different sizes to add to the media. Small particles (30 ± 15 nm) and large particles (45 ± 17 μm) were dispersed at a concentration of 1 wt.% and sterilized in the MEB, which was then inoculated and incubated for pellet growth. As the particles were adsorbed into the mycelial network, the media returned to a pale color, and the pellets visibly took up the color of the additive, as seen in Figure 2d. However, there are many ideas on the mechanism(s) behind particulate adsorption into fungal pellets.

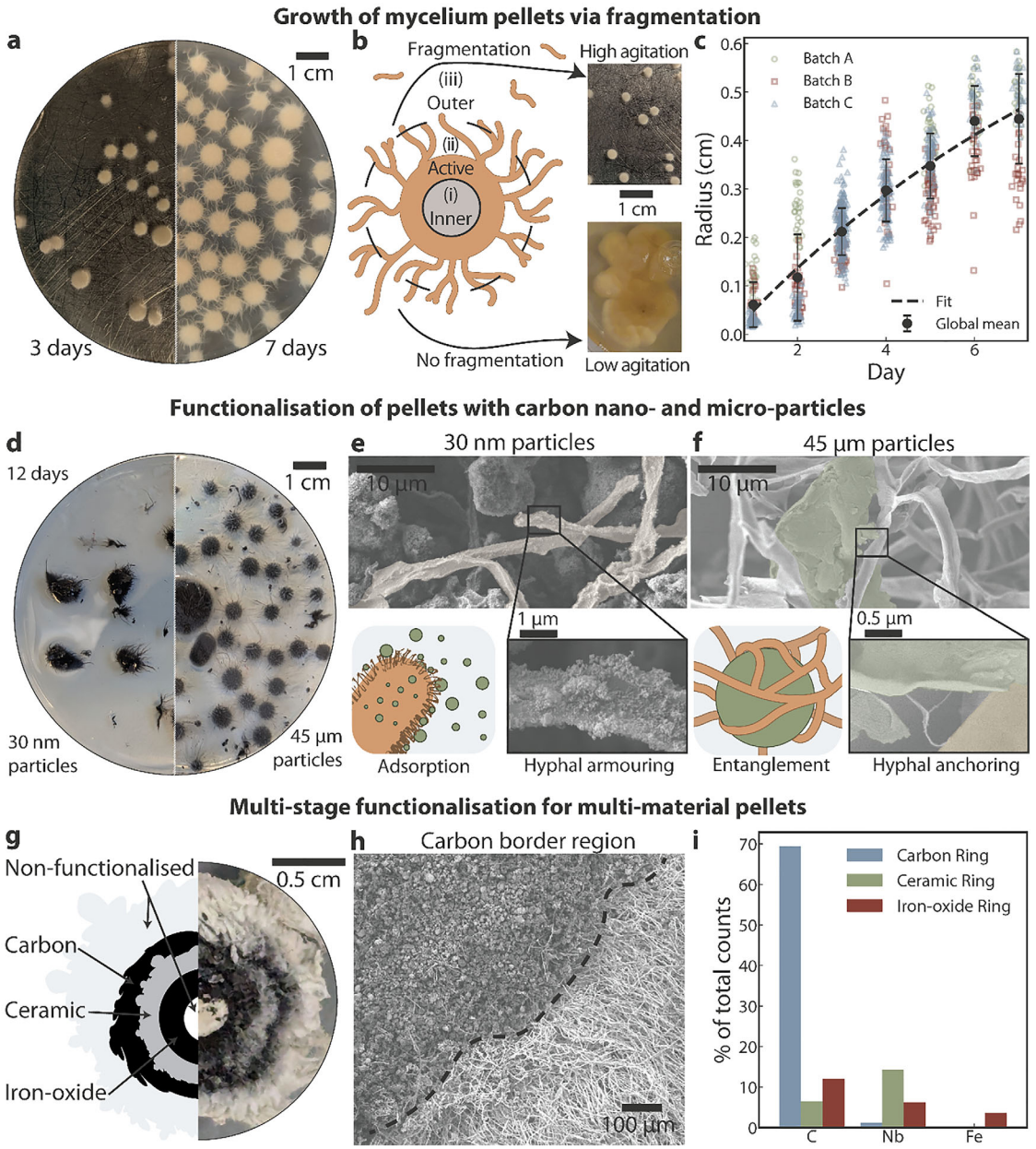

FIGURE 2 | Fungal pellet formation and growth. (a) Images of pellet development at three and seven days show an increase in size and a hairy outer shell. (b) Schematic of a mycelium pellet and its zones of growth (i) inner, starvation ring, (ii) active growth ring, and (iii) outer hyphal ring. Agitation of the culture controls pellet formation: high agitation yields small pellets, while low agitation yields a single pellet. (c) A plot of mycelium pellet radii for three separate batches over seven days of incubation fitted to a growth model of fungi growth (dashed line), where $R^2 = 0.92$. The global mean is defined as the mean of the diameter for pellets from all batches, and error bars represent the standard deviation. (d) Carbon particles with increasing sizes, 30 ± 15 nm and 45 ± 17 µm, are adsorbed into the mycelium pellets over time. Images of carbon-mycelium pellets after twelve days of incubation show the final pellet morphology. (e) SEM images of carbon-mycelium pellets show that 30 nm particles aggregate into large (>2 µm) clusters as well as adsorb along the hyphae (false-colored brown), creating an armoring effect, shown in the inset. (f) SEM images of pellets with large particles show that the particles (45 µm, false-colored green) are enveloped within the fungal network and trapped via entanglement. The inset shows bridges between the fungal cell wall and the particles, possibly acting as an anchoring mechanism. (g) Multi-functional pellets prepared by the incremental addition of particles over the growth period exhibit distinct rings of different particles, including carbon, ceramic, and iron oxide, depicted in the schematic and corresponding optical image. (h) SEM images of the border region reveal a distinct point (dashed line) at which the pellet collected all particles from the media and continues to grow normally. (i) A plot summarizing the percent of extracted EDX counts by elemental carbon (C), niobate (Nb), and iron (Fe) for the carbon-based, niobate-based ceramic, and iron oxide rings, respectively. Each ring corresponds well with the elements derived from the particles adhered during that time.

In a shaking culture, particle transport toward the pellet surface is dominated by advection, with Peclet numbers far exceeding unity ($Pe >> 1$) for all particle sizes. As a result, the migration of particles to the pellet is rapid, and the limited step for adsorption is instead governed by the sticking forces in the system. These could include van der Waals interactions, electrostatic attraction (or repulsion), chemical adsorption, and mechanical interlocking within the mycelium network [16]. Although electrostatic forces are often considered the most intuitive mechanism, our measurements show that the zeta potential for pellets increases from −17 mV to approximately zero mV after three days of cultivation, while remaining negative (−12 mV) for hyphal fragments (Figure S3), similar to other reported values for mycelium [16, 49]. Given that the particles used in this study are also negatively charged, electrostatic attraction alone cannot explain the observed adsorption and the resulting changes in pellet morphology. Other mechanisms, or combinations of them, are likely to play a significant role in the adhesion of particles to the fungal hyphae.

The overall morphology of the pellets differs from that of their non-functionalized counterparts. With the addition of nano- and micro-particles, some pellets sediment under gravity, developing into oblong and non-spherical shapes with a broader range of diameters, as shown in Figure S4. To understand where the particles end up, Figure 2e shows SEM from a pellet grown in the presence of 30 nm particles. Here, we can see hyphae present as well as large aggregations of the particles dispersed throughout, further supporting SEM are shown in Figure S5. A closer look at the surface of the hyphae reveals an armor-like effect as the nanoparticles adsorb directly to the hyphal cell wall. For much larger particles, Figure 2f shows an SEM of 45 μm particles, which become physically entangled within the mycelium network. These particles are often seen with small fibrous attachments extending from the cell wall to the particle surface. Figure S6 shows a dramatic example of this anchoring phenomenon. We speculate that extracellular matrix (ECM) components, including surface exposed proteins and polysaccharides, become partially detached and subsequently adhere to the particle surface. Fungi are known to secrete extracellular polysaccharides, such as β-glucans, which facilitate the transport of active components in the surrounding medium and facilitate the binding of enzymes, proteins, and metal ions [50]. These extracellular polysaccharides can interact non-covalently via the formation of salt bridges and ionic bonding, which may also enhance particle-hyphae attachment and stabilization [10, 51, 52]. Additionally, the secretion of extracellular polysaccharides into the medium is known to modify local viscosity and reduce friction at the cell-substrate interface, which may also promote particle entanglement. As the pellet density increases with particle addition, stronger pellet-particle and pellet-pellet interactions, coupled with the hydrodynamic shear, may contribute to the fragmentation of the pellet, resulting in the appearance of an overall smaller pellet [41, 44, 53] Therefore, these particle-mycelium interactions not only reshape the pellet morphology but also enable the control of the material composition during growth.

To prepare a multi-material fungal pellet, we sequentially introduced three types of particles into growing mycelium pellets over a period of twelve days, adding a new particle type every four days. The first addition consisted of iron oxide nanoparticles (50 ± 10 nm), followed by ceramic niobate-based particles (50 ± 25 μm), and finally 30 nm carbon particles. Figures S7 and S8 shows how the pellets appear during and after this process. We aimed to create distinct functional rings within each pellet. Achieving this required controlling pellet fragmentation, as excessive fragmentation of the hyphae in the later stages would produce new pellets containing only one or two types of particles. To prevent this, we decreased the agitation in the system to reduce the shearing of outer hyphae.

Figure 2g shows an optical cross-section of a fully-grown multi-material pellet, revealing five distinct regions, corresponding to pure mycelium and rings functionalized with carbon, ceramic, or iron-based particles. Once most particles were adsorbed into the network, the mycelium resumed normal growth, completely encapsulating the different material layers. This relatively sharp transition between the functionalized and non-functionalized rings is further illustrated in the SEM image shown in Figure 2h. To verify the composition of these rings, we performed energy-dispersive X-ray spectroscopy (EDS), as shown in Figure S9. The resulting spectra confirm that each ring exhibits distinct and expected elemental signatures, demonstrating spatial separation and control of the different particle types within a single pellet, summarized in Figure 2i. In principle, these multi-functional pellets, particularly those with a magnetic iron-oxide core, could be used in applications that require retrievable or externally manipulable materials through non-contact methods, offering a promising route to reusable biohybrids with multiple functionalities. Nevertheless, the current pellets remain relatively fragile and susceptible to deformation during handling, indicating that additional processing steps are required to produce functional materials.

2.2 | Hierarchical Structuring of Fungal Biohybrids through 3D Printing

3D printing provides precise control over the spatial organization of engineered living materials, allowing for the deposition of bioinks in architectures that influence cell growth and function. *G. Lucidum* spawn and active hyphal fragments were mixed with κ-carrageenan, sodium alginate, agar, and cellulose-based thickener, then 3D printed by direct extrusion and deposited in a layer-by-layer fashion. The previous fungal bioink [36] lacked a cross-linking agent, which is essential for maintaining structural integrity during mycelial growth in liquid culture, as a non-crosslinked hydrogel would readily dissolve in the medium. Therefore, we formulated an ink based on a similar composition previously used to support an ELM containing microalgae [54], where sodium alginate was cross-linked with Ca^{2+} ions to stabilize the printed construct.

To maintain mycelium growth from the printed surface, we reduced agitation by using 50 mm-diameter cups and shaking at 100 rpm to lower fragmentation rates, allowing the mycelium to continue growing submerged in the media while minimizing the formation of secondary pellets. As the mycelium grows outward from the printed geometry, we expect rounding of the corners and edges. To investigate this effect, we 3D print a simple 20 mm × 20

mm × 5 mm grid and overgrew it with mycelium. In the case of a square rounding, the shape can be described by a superellipse:

$$\left|\frac{x}{a}\right|^n + \left|\frac{y}{b}\right|^n = 1$$

where a and b are the semi-axes of the superellipse and $n = 2$ corresponds to an ordinary ellipse, $n > 2$ produces a rounded square, $n = 1$ yields a rhombus, and $0 < < 1$ gives a shape with pointed corners and convex sides. Figure S10 shows a sketch with a and b labelled for $n = 0.95$, 2, and 5.

Figure 3a shows optical images of the 3D printing process at key steps. The as-printed shape (i) exhibits slightly convex edges, similar to the crosslinked version (ii). Fitting a superellipse to the outlines yields $n = 0.94$ for the as-printed shape and $n = 0.95$ for the crosslinked shape. As mycelium grows into the nutrient broth, the hyphae extend away from the surface into the medium, gradually rounding the geometry following pellet formation. After four days, the shape (iii) evolves where $n = 4.94$. After eight days (iv), with the addition of 30 nm carbon particles for the last four days, further shape smoothing occurs, reducing n to 1.77 and approaching an elliptical form. As the 3D-printed shape encloses the mycelium well, it may be possible to control which parts of the mycelium have access to nutrients or functional agents. When we compare the trends in the shape parameter n across the printing and growth processes in triplicate, Figure 3b shows that n is relatively stable just below 1 (a rhombus) before growth, then the shape rounds as the mycelium grows from the hydrogel surface. We observed three samples, each with or without functionalization, at four and eight days. In both cases, n reached above three (a rounded square) before decreasing toward two (an ellipse). Similarly, Figure 3c shows that the semi-diameters, a and b, decrease slightly after crosslinking as the gel contracts. After growth begins, the (hydrodynamic) semi-diameter increases over time.

We studied the rheological behavior of the bioink by investigating the flow behavior and recovery at room temperature. For the bioink (Figure 3d), the storage modulus (G′) exceeds the loss modulus (G″) at lower shear rates, followed by a decline in both. The yield point, the shear stress at the limit of the linear viscoelastic region, was on average 92 ± 4 Pa. The flow point, where G′ = G″, was on average 353 ± 42 Pa across three replicate bioink samples, similar to the reported values for the cellulose-alginate bioink this work was based on [54]. The ink itself is shear-thinning, Figure S11. To determine the ink's recovery profile, we select a high shear rate ($(\dot{\gamma} = 10)$ s^{-1}) to simulate the stresses applied during the printing process. We measured recovery using a low-amplitude oscillatory sweep with a high-shear step for 20 seconds, highlighted in red in Figure 3d. Immediately after this high shear, the ink begins recovering over the following minutes.

We investigated the ability to selectively functionalize living 3D prints by controlling particle deposition via gelatin encapsulation. Mycelium-laden grids were embedded in gelatin, as shown in Figure 3f, and the gelatin solidified around the structure with minimal damage to the existing mycelium network. A layer of particle-containing media was then added on top of the gelatin layer, limiting the mycelium available for functionalization.

Over several h, gelatin undergoes swelling and partial liquefaction, diffusing into the particle layer (Figure S12) and slowing the diffusion of the dispersed particles as calculated in Figure S13. Consequently, as gelatin diffuses, particles become trapped in the viscous medium, slowing the rate of particle deposition. Figure 3g illustrates that encapsulation results in varying degrees of particle deposition over time. Within the first few hours, the deposition areas are defined by hard lines between non-functionalized and functionalized mycelium. As time passes, a gentler gradient forms on the mycelium's surface.

By utilizing these different regions, we can generate various types of functional materials with gradient depositions. SEM images, shown in Figure 3h, reveal that particles disrupt the outer mycelial layer, especially in areas exposed to the particle media for longer periods and higher up on the print surface. In contrast, particle counts averaged across 0.1 mm^2 surface areas from one sample confirm the gradient quantitatively (Figure 3i), with the gelatin line at 10 mm showing a clear difference in deposition. On the other hand, by keeping the deposition time low at 2–4 h, we can create shape-smart functionalization by selectively masking areas, as shown in Figure 3j and Figure S14. These results demonstrate that combining 3D printing, controlled growth, and spatially selective functionalization can establish a platform for engineered living materials with tunable, spatially resolved properties.

2.3 | Biohybrid Fungal Materials

Many organisms are known for their electrical excitability and signaling, often associated with rapid responses to environmental stimuli. For instance, plants exhibit long-distance electrical signaling, in which action potentials, resulting from rapid changes in membrane voltage as ions flow across the cell membrane, mediate stress responses and movement behaviors [55]. Mycelium bioelectric signals similarly arise from the activation of selective ion channels and pumps that regulate the transport of Na^+, Ca^{2+}, and K^+ across the membrane [56–58]. These transmembrane processes, while primarily serving physiological functions, can also generate measurable electrical fluctuations.

At the macroscale, mycelium networks are expected to exhibit electrical behavior across interconnected cells, which can be harnessed for sensing applications or as active feedback components in biohybrid systems [59–61]. In biohybrid technologies, similar principles have been leveraged to integrate biological processes directly into functional devices. For example, plant-based biohybrids with conductive, enzymatically modified roots have been engineered to harvest electrical energy from root secretions such as glucose [62]. In our case, the inclusion of conductive carbon black within mycelium may enhance charge transport throughout the network.

To investigate the effects of adding functional nanoparticles on our ability to collect bioelectric signals from the mycelial network, we 3D-printed grid-based struts as a scaffold for the mycelial network. Each strut measured 40 mm × 5mm × 5 mm. Figure 4a shows images of the (i) printing, (ii) growth, (iii) functionalization, (iv) sterilization, and (v) measurement process for the samples. After printing a grid, they are crosslinked in a

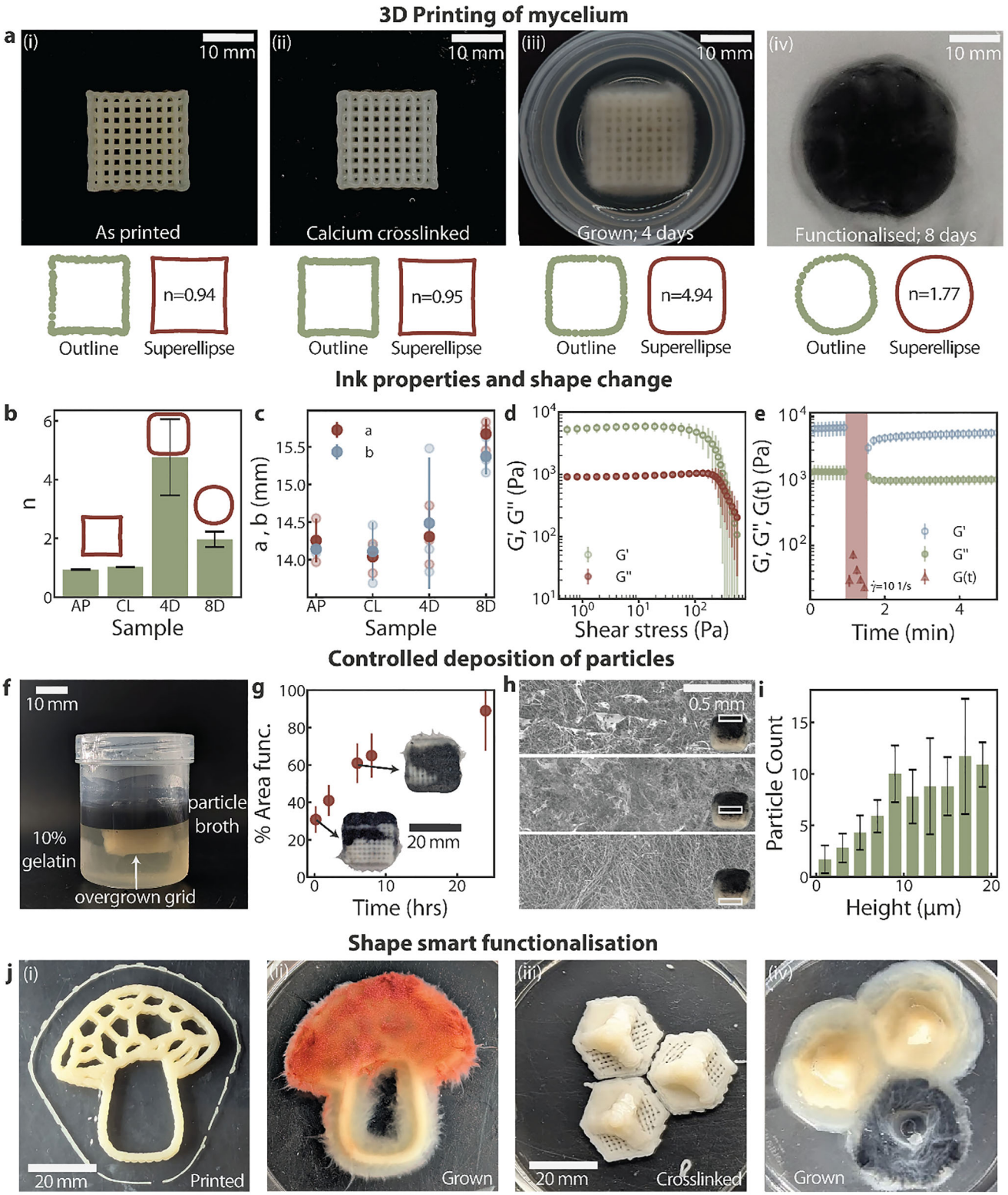

FIGURE 3 | Hierarchical structuring of fungal biohybrids through 3D printing. (a) Microgranular mycelium-laden hydrogel ink is printed via direct ink writing into (i) 20 × 20 mm grids, where the 2D shape deviates from a designed square to a superellipse with concave sides. (ii) The print is submerged in a calcium chloride solution to initiate alginate crosslinking. (iii) The crosslinked grid is put in MEB to provide nutrients for the mycelium colony and allow growth, resulting in soft, hair-like morphology at the surface of the grid. This growth rounds the corners and makes the sides convex. (iv) A particle slurry added to the MEB functionalizes the growing hyphae, forming a shaped biohybrid material while further rounding out the shape as growth continues. (b) The 2D projection of at least three printed grids fitted to a super ellipse, $|x/a|^n + |y/b|^n = 1$, show the evolution of the grids during processing for the shape parameter, n, and (c) the semi-diameters a and b for the as printed (AP), calcium crosslinked (CL), 4 days of growth (4D), and eight days of growth (8D) samples. (d) The storage (G′) and loss modulus (G″) over shear stress for the bioink. At low shear rates, G′ is greater than G″,

5% $CaCl_2$ solution for 15 min, then washed and incubated for 4 days in either a plain or a 1 wt.% MEB solution containing 30-nm carbon black. As controls, we sterilized both types of samples via an autoclave cycle to terminate the biological activity. Once grown, the struts are removed from the media, washed, and placed on an indium tin oxide (ITO)-based electrode setup capable of recording electrical signals. Since the expected voltages are typically below one mV and highly sensitive to environmental fluctuations, all measurements were conducted within a Faraday cage. Samples were prepared in a sterile chamber containing a small water reservoir to maintain humidity during growth. After equilibration, we expect the mycelium to make direct contact with and grow across the electrode surface, as confirmed post-experiment in Figure S15, which shows that as fresh mycelium grows, a new white layer devoid of carbon particles forms.

The differential signals shown in Figure 4b exhibit little activity for sterilized (dead) mycelium struts for both non-functionalized and functionalized samples. In all samples, peaks arise near the beginning of the measurement (between zero and 3 h), which can be attributed to the relaxation of the hydrogel and mycelium. After approximately 8 h, the signal shows bioelectric-like spiking in both living samples (non-functionalized and functionalized). With an apparent higher amplitude for both positively and negatively polarised peaks within the functionalized sample.

To examine the comparison between the functionalized and non-functionalized samples in detail, we extract peak information after subtracting long-term drift within the samples. Here, we observe that the functionalized sample exhibits an increased amount of higher-amplitude positively and negatively polarized peaks (Figure 4c). Often the positive and negatively polarized peaks are followed immediately by the other, indicating a polarization/depolarization-like effect. Figure S16 shows the identified peaks and their corresponding average waveform, where this effect is observed. We also notice that the average amplitude of the observed peaks in the functionalized sample is 9-fold larger for the positive and 10-fold larger for the negative peaks. This enhanced response suggests that functionalizing conductive carbon within the mycelium improves the electrical connectivity of the living network.

To investigate this effect, we calculate the signal-to-noise ratio (SNR) of the samples by treating the first hours (2.5–8) of the data set as the noise, before the mycelium has equilibrated and started growing over the electrode surface. The signal arises after eight to 10 h, when the first observable bioelectric peaks appear within the samples. Over the whole frequency range, the dead sample generates no observable signal with a root-mean square of $(SNR_{RMS}) > 0$ dB. The non-functionalized sample has a reliable SNR_{RMS} of 10.46 dB, which is significantly lower compared to its functionalized counterpart, whose SNR_{RMS} is 27.90 dB. As fungal bioelectric signals are commonly found in the 0.1–5 Hz range, we estimate the power spectral density (PSD) of the noise and signal segments via Welch's method [63] and calculate the SNR per frequency, shown in Figure 4f. This shows a clear increase in the SNR for the functionalized sample over the signal range of interest for the bioelectric behavior of mycelium.

To understand why we see an improvement in the signal for functionalized samples, we measured the real part of the impedance (Zp') for samples with one day of functionalization (low loading) and five days of functionalization (high loading), shown in Figure S17. All samples had five days of mycelium growth within the liquid culture. We normalized the Zp' of the samples to a non-functionalized sample via

$$\Delta Z_p{}' / Z'_{p(\text{non-func})} = \left(Z'_{p(\text{sample})} - Z'_{p(\text{non-func})} \right) / Z'_{p(\text{non-func})}$$

Figure 4g shows a clear trend: as the loading increases, the real part of the impedance decreases significantly. Therefore, carbon black functionalization lowers the impedance, which may support more efficient extracellular electron transfer throughout the mycelial network [64]. In this regard, particle functionalization not only modifies the network's morphology but also imparts, in this case, tunable electrical properties, establishing a path for responsive biohybrid fungal materials for sensing.

We can move beyond a simple strut geometry by creating modular building blocks, such as tessellating pyramidal units. By functionalizing these units individually, the impact of contamination or poor growth on the overall structure can be minimized, as underperforming blocks can be selectively replaced. The blocks nest together, as shown in Figure 4f, and as they grow, they establish connections between the two blocks across the electrode setup and exhibit bioelectric signals. Together, the assembled blocks can sustain growth for several days, as shown in Figure S18. When the bioelectric signal begins to decay, an underperforming block can be substituted with a fresh unit, immediately rejuvenating the signal across the mycelial network, as shown in Figure 4g. By utilising both the shaping freedom and functionalization of the mycelium, we can design adaptive structures that can be updated and replaced in response to diminished performance.

while higher shear stress results in flow of the ink. (e) Elastic recovery of the bioink is measured by measuring a "rest" state at a shear strain within the linear viscoelastic region ($\gamma = 1\%$) and applying high deformation, ($\dot{\gamma} = 10$), indicated by the region in red. (f) Areas of the fungi are isolated by locking them in gelatin to expose selected areas to a particle slurry. The exposed fungi will still uptake particles when added, and over time, the gelatine swells and liquifies, allowing for retrieval. (g) As the gelatin diffuses into the media, the printed piece is more exposed to the dispersed particles, and the functionalized area increases. Optical images are shown as an inset. (h) SEM images over the printed mycelium's height show a gradient of particles, the inset optical image shows roughly the area the SEM images were collected. (i) After counting particles located on the surface (visible in SEM) for several images from different z-positions. There are very few particles are observed on the print's surface near the bottom (longest covered in gelatin) area of the mycelium. (j) This method is used to selectively adsorb particles into the mycelium network based on their shape, as shown in the optical image of a (i) printed mushroom with the (ii) mushroom cap functionalized with red ceramic particles. Shapes tailored to generate (iii) building blocks or lattices can be (iv) independently functionalized and assembled during a final growth phase to form replaceable and tailorable structures.

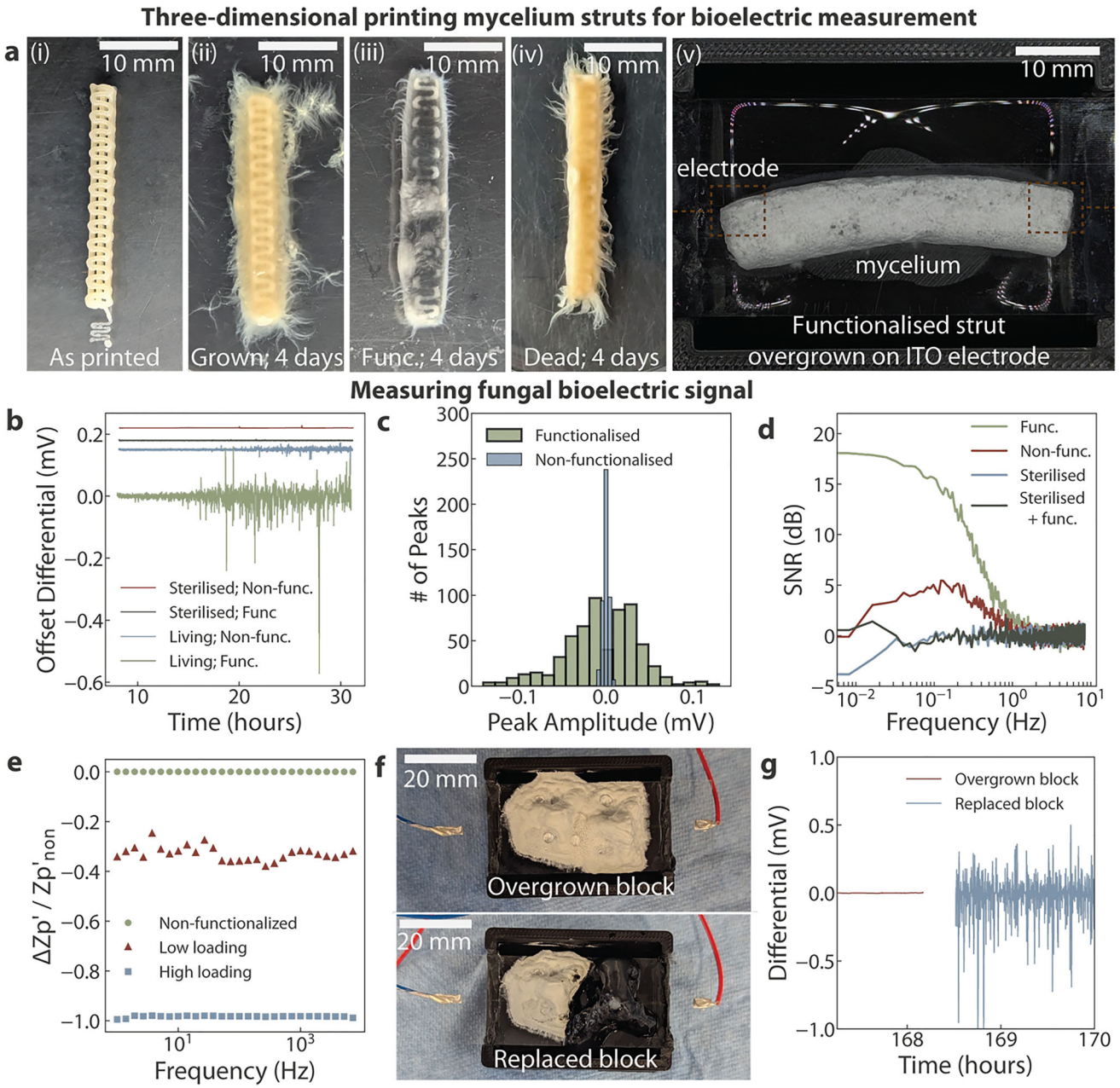

FIGURE 4 | Fabrication of a biohybrid fungal material. (a) Optical images of strut preparation for bioelectric measurements of (i) as printed, (ii) grown and (iii) functionalized for four days, and (iv) sterilized (dead) after growth. Printed grids offer ample surface area for mycelium growth and functionalization throughout the volume, rather than just along the surface. The printed core also helps maintain the mycelium's shape throughout the measurement and growth stages. (v) Patterned ITO electrodes are prepared using photolithography on glass, and the mycelium print is placed between these electrodes. As the hyphae grow and connect to the electrode, we measure the bioelectric signal. Eventually, the mycelium growing at the air interface forms a white skin. (b) The extracted, drift corrected, and y-offset differential for a sterilized (dead) and living non-functionalized and carbon functionalized mycelium struts. (c) A histogram of the amplitudes for the two living samples over 20 h of the measurement. (d) Investigation of the signal-to-noise ratio (SNR) for the sample types over frequency. (e) Reduction in impedance (real part, ΔZp') of the samples with low loading (1 day in particle dispersion) and high loading (4 days in particle dispersion), normalized to the impedance of the non-functionalized sample. (f) Mycelium lattice-like blocks allow for replacement during a measurement, for instance, to remove a poorly performing block. (g) The replaced block immediately shows a return of bioelectric signal in the differential measurement.

3 | Conclusion

We observed that pellet formation relies on the hydrodynamic forces within the culture, and the attachment of particles varies depending on their size, shifting from the armouring of hyphal cell walls to the physical entanglement in the mycelium, with bridging of particles to the cell wall. We find that 3D printing can spatially control growth within a liquid culture without compromising biological activity, enabling growth-mediated functionalization of designed structures. Together, these insights

expand a fabrication approach in which the living network gains multi-functionality through its living network and functional assembly method. By linking particle-mycelium interactions with fabrication control via 3D printing, we provide a new design for fungal-based living materials. This approach establishes mycelium as both a bio-factory and a structural scaffold to prepare self-organised, adaptive, functional living materials. More broadly, these findings point toward a future in which autonomous, adaptive, and multifunctional materials can be created through the directed growth of living systems.

4 | Experimental Section/Methods

4.1 | Materials

The following chemical were purchased and used as received: Gibco Bacto Malt Extract (Fisher Scientific), peptone (Merck Sigma), calcium chloride anhydrous (Merck Sigma), conductive carbon black 30 and 148 nm and graphite (Nanografi Nano Technology), sodium alginate (Merck Sigma), agar-agar (Carl Roth), κ-Carrageenan (Merck Sigma), iron (II, III) oxide nanopowder (Merck Sigma). A cellulose-based thickener (MCG, Vivapur MCG 811 P) was provided by JRS Pharma. Ceramic niobate-based particles were kindly provided by S. Ammu and S. Sharma [65, 66]. The fungal species *Ganoderma lucidum* (strain number M9726) was purchased from Mycelia NV.

4.2 | Growth of Fungal Pellets

A two-stage process prepares fungal pellets. The fungus was transferred onto malt extract agar (MEA) to prevent contamination and for visual control. MEA plates were inoculated and incubated at 27°C for 7 days and stored at 4°C. Two rectangles (5 mm × 10 mm) are cut from the agar and inoculated into a 250 mL Erlenmeyer flask containing 150 mL of malt extract broth (MEB). The flask is then vigorously shaken to loosen the hyphal tips. The seed is incubated for 7 days at 27°C, shaking at 160 rpm. The seed inoculum is then washed three times from MEB into 25 mL of sterile DI water in 50 mL Falcon tubes. Vortexing the pellets for 1 min breaks them up into smaller hyphal fragments for reseeding, and these fragments are then stored at 4°C. Pellets prepared for growth or functionalization are inoculated with 1 mL of seed solution and incubated at 27°C for 7–14 days. Nano- and microparticles are added to MEB at 1 wt% and sterilized via an autoclave cycle (Hirayama HG-50) at 115°C for 15 min before inoculation. Fungal pellet formation is tracked via optical imaging by collecting 15+ pellets in a sterile petri dish at set time periods. The dry weight of pellets over the growth period is determined by collecting all biomass from a 150g sample, freezing it at -80°C for at least 3 h, and then lyophilizing it.

4.3 | Mycelium Bioink Preparation

Mycelium-inoculated bioinks were formulated in DI water containing 1.5 wt% sodium alginate, 3 wt% κ-carrageenan, 5 wt% cellulose-based thickener, and 1.5 wt% agar, following with slight modifications ref. [54]. The sodium alginate was dispersed into hot (~60°C) water, mixed with a liquid frother attached to a hand rotary tool (Proxxon, No 28505–11) at 5,000 rpm for 30 seconds and rested for 10 min. The remaining additives were mixed individually for 1 min in the following order: cellulose-based thickener, κ-carrageenan, and agar, yielding a paste-like mixture. The bioink was sterilized via autoclave (Hirayama HG-50), at 121°C for 20 min. As the ink cools from 50°C to room temperature, it was mixed for 1 min every 5 min under sterile conditions of a biosafety cabinet (Herasafe). This step forms microgranules as the agar sets, critical for direct ink writing. Living mycelium grown in liquid culture was harvested as a seed inoculum outlined above, and 1 mL of these mycelial fragments for every 50 mL of ink was mixed into the bioink. The bioink was loaded into 20 mL syringes and degassed via centrifugation at 1690 g for 1 min. The bioink was typically used immediately for direct ink writing or stored, sealed at 4°C, when not in use, to inhibit mycelial growth before printing.

4.4 | Rheology of the Inks

The rheological properties were determined using a rotational rheometer (Anton Paar, MCR302e). Approximately 1 g of bioink was positioned between a 20 mm-diameter serrated top plate and a sandpaper-covered bottom plate, with a 1.2 mm gap, to prevent wall slip. Shear storage and loss moduli were determined via an amplitude sweep at a fixed frequency of 1 Hz. The yield point was defined as the end of the linear viscoelastic region (LVE), and the flow point was the point at which the storage and loss moduli were equal. The elastic recovery of the bioink was measured using a time-dependent oscillatory test with a high-shear interval. To simulate at-rest behavior, the amplitude sweep was performed at a low shear stress within the LVE ($\gamma = 1\%$) for 1 min, followed by a high shear stress ($\dot{\gamma} = 10$) for 20 s to simulate the time scales and stresses applied during printing. The recovery was then measured using a low-amplitude sweep for 5.5 min.

4.5 | Direct Ink Writing

Printed components of this work were prepared on a modified Ultimaker 2+ desktop 3D printer as described in ref. [67]. Designed patterns were sliced with PrusaSlicer, with printing and travel speeds set to 15 mm s^{-1} and 30 mm s^{-1}, respectively, and a layer height of 0.7 mm for a nozzle diameter of 0.84 mm. The resulting prints were submerged in 5% $CaCl_2$ for 10 min to cross-link the sodium alginate within the hydrogel. The prints were incubated in sterile 50 mm-diameter polypropylene (PP) cups containing 10 mL of MEB, either with or without nano- and microparticle additives, under shaking at 160 rpm and 27°C for 4–8 days.

4.6 | Characterization

SEM samples were sputter-coated with a ~10 nm layer of gold using a Quorum Q300T D Sputter Coater. Imaging was performed on a JEOL JSM-7500F Field Emission Scanning Electron Microscope. Zeta potential measurements were performed on shredded mycelium and mycelium pellets over the growth period of one to seven days in a disposable cuvette (DTS1070) using a Malvern Zetasizer Nano ZS.

4.7 | Electrode Fabrication

Indium tin oxide (ITO)-coated (thickness: 100 nm; sheet resistance ~14-20 Ω sq-1) glass slides (25 mm × 75 mm × 1.1 mm) were procured from Ossila, UK (Product code: S281-20), and used as received. The desired ITO electrode patterns were achieved using photolithography [68]. First, the ITO-coated glass substrate was cleaned with acetone, isopropyl alcohol (IPA), and deionized (DI) water, followed by dehydration on a hotplate at 110 °C for 1 min. A thin layer of positive photoresist (AZ 1518; Microchemicals GmbH) was then spin-coated (@4000 RPM; 30s) on top of the ITO layer using a spin-coater (WS-400B-6NPP/LITE; Laurell Technologies, USA). The coated substrate was then pre-baked on a hot plate at 100 °C for 1 min to evaporate any remaining solvent and prevent the photoresist from sticking to the photomask. The photomask contained two square pads (5 mm × 5 mm) placed 30 mm apart, and each connected to the outer/end pads (5 mm × 2 mm) using a thin strip (13.5 mm × 1 mm), shown schematically in Figure S19. Next, for pattern transfer, the coated substrate was covered with the photomask and exposed to UV light (Omnicure S1500 UV-lamp; Lumen Dynamics) for 10 seconds. Post exposure, the substrate was immersed in a beaker containing positive photoresist developer (AZ 726 MIF; Microchemicals GmbH) with the coated side facing up, stirred gently for ~ 60 seconds. This caused the unmasked photoresist to dissolve completely in the developer while the masked region remained intact. Next, the unwanted ITO layer was etched away by immersing the substrate in diluted hydrochloric acid (HCl, 1:6 in H_2O) and sprinkling zinc (Zn) dust evenly across the entire substrate [69, 70]. This caused the unmasked ITO to etch away while the masked ITO region was protected by the photoresist coating. Finally, the etched substrate was thoroughly cleaned in acetone, IPA, and DI water, followed by dehydration at 110°C for 2 min to obtain the patterned ITO electrode. Electrical connections were made using two wires in contact with the ITO outer/end pads, and silver-loaded epoxy (8331D-14G; Farnell Nederland) was used as the adhesive.

4.8 | Bioelectric Measurements

We prepared 40 × 5 × 5 mm^3 printed grids grown for four days in MEB with and without 1 wt.% 150 ± 30 nm conductive carbon particles. The resultant soft grid was washed three times with sterile DI water and placed across the two electrodes. The electrodes were connected to a data logger (PicoLog ADC-20; Pico Technology) with a 60 ms conversion time. Measurements were conducted for three days, allowing a fresh layer of mycelium to form on the surface of the struts and electrodes. Dead controls were generated from the non-functionalized fungal grid by sterilization in an autoclave. Raw differential-voltage data were extracted from the HDF5 files and segmented into noise (no growth, equilibration) and growth (signal) periods, corresponding to 2.5–6 h and ≥10 h of measurement time, respectively.

The broadband signal-to-noise ratio (SNR) was calculated via the standard method as

$$SNR_{RMS} = 20log_{10}\frac{\mu}{\sigma}$$

where μ is the mean signal amplitude and σ is the standard deviation of the noise. Welch's method was used to estimate the power spectral density (PSD), *P(f)*, for both signal and noise. The frequency-dependent SNR was then computed by integrating the SNR over frequency.

4.9 | Impedance Measurements

Impedance spectra were acquired using a broadband dielectric spectrometer (Novocontrol Technologies GmbH) over a frequency range of 10^{-1}-10^7 Hz. The real component of the impedance, Z'_p, was measured for different sample conditions: non-functionalized, low loading, and high loading.

Acknowledgements

This project was funded by the European Union (ERC Consolidator Grant, AM-IMATE, 101088968). We would also like to thank Satya Ammu and Saurav Sharma for providing us with their ceramic niobate-based particles, as well as the Advanced Soft Matter section in the Department of Chemical Engineering at TU Delft, and Sietse Kuipers for access to and assistance with zeta potential measurements.

Funding

ERC Consolidator Grant, AM-IMATE, 101088968

Conflicts of Interest

The authors declare no conflict of interest.

Data Availability Statement

The data that support the findings of this study are openly available at the following URL/DOI: https://doi.org/10.4121/688d5cbe-8438-4051-a6df-3723fd8ffb12. ref. [71].

References

1. M. E. Voutetaki and A. C. Mpalaskas, "Natural Fiber-Reinforced Mycelium Composite for Innovative and Sustainable Construction Materials," *Fibers* 12 (2024): 57.

2. S. Motamedi, D. R. Rousse, and G. Promis, "A Review of Mycelium Bio-Composites as Energy-Efficient Sustainable Building Materials," *Energies* 18 (2025): 4225.

3. N. Verma, S. E. Jujjavarapu, and C. Mahapatra, "Green Sustainable Biocomposites: Substitute to Plastics With Innovative Fungal Mycelium Based Biomaterial," *Journal of Environmental Chemical Engineering* 11 (2023): 110396.

4. V. Whabi, B. Yu, and J. Xu, "From Nature to Design: Tailoring Pure Mycelial Materials for the Needs of Tomorrow," *Journal of Fungi* 10 (2024): 183.

5. E. Elsacker, M. Zhang, and M. Dade-Robertson, "Fungal Engineered Living Materials: The Viability of Pure Mycelium Materials with Self-Healing Functionalities," *Advanced Functional Materials* 33 (2023): 2301875.

6. S. Schyck, P. Marchese, M. Amani, et al., "Harnessing Fungi Signaling in Living Composites," *Global Challenges* 8 (2024): 2400104.

7. A. V. Hernando, W. Sun, and T. Abitbol, ""You Are What You Eat": How Fungal Adaptation Can Be Leveraged toward Myco-Material Properties," *Global Challenges* 8 (2024): 2300140.

8. N. Nussbaum, T. von Wyl, A. Gandia, E. Romanens, P. A. Rühs, and P. Fischer, "Impact of Malt Concentration in Solid Substrate on Mycelial Growth and Network Connectivity in Ganoderma Species," *Scientific Reports* 13 (2023): 21051.

9. K. Engelbert, C. Deffur, T. C. Cairns, et al., "Adjusting Aspergillus Niger Pellet Diameter, Population Heterogeneity, and Core Architecture During Shake Flask Cultivation," *Biotechnology for Biofuels and Bioproducts* 18 (2025): 62.

10. A. Sinha, L. G. Greca, N. Kummer, et al., "Living Fiber Dispersions from Mycelium as a New Sustainable Platform for Advanced Materials," *Advanced Materials* 37 (2025): 2418464.

11. H. Sarma, P. N. Bhattacharyya, D. A. Jadhav, et al., "Fungal-Mediated Electrochemical System: Prospects, Applications and Challenges," *Current Research in Microbial Sciences* 2 (2021): 100041.

12. K. Li, Z. Wei, J. Jia, et al., "Engineered Living Materials Grown From Programmable Aspergillus Niger Mycelial Pellets," *Materials Today Bio* 19 (2023): 100545.

13. H. Wang, W. Wang, J. Tao, S. Liu, X. Hou, and C. He, "Anchoring Mycelium on CNTs to Make Strong and Smart Self-Regenerative Composite Materials," *Composites Part B: Engineering* 287 (2024): 111861.

14. Z. Li, X. Deng, G. Chen, Z. Zhang, J. Han, and X. Lu, "Mycelium-Derived Self-Healing Electrodes for High-Performance and Biodegradable Supercapacitors," *Chemical Engineering Journal* 524 (2025): 169372.

15. N. Attias, M. Reid, S. C. Mijowska, et al., "Biofabrication of Nanocellulose–Mycelium Hybrid Materials," *Advanced Sustainable Systems* 5 (2021): 2000196.

16. X. Fu, S. Zhang, X. Zhang, et al., "Sustainable Microplastic Remediation with Record Capacity Unleashed via Surface Engineering of Natural Fungal Mycelium Framework," *Advanced Functional Materials* 33 (2023): 2212570.

17. W.-K. Zhu, H.-P. Cong, Q.-F. Guan, et al., "Coupling Microbial Growth with Nanoparticles: A Universal Strategy To Produce Functional Fungal Hyphae Macrospheres," *ACS Applied Materials & Interfaces* 8 (2016): 12693–12701.

18. Z. Molnár, V. Bódai, G. Szakacs, et al., "Green Synthesis of Gold Nanoparticles by Thermophilic Filamentous Fungi," *Scientific Reports* 8 (2018): 3943.

19. S.-M. Wu, Y. Su, R.-R. Liang, et al., "Crucial Factors in Biosynthesis of Fluorescent CdSe Quantum Dots in *Saccharomyces cerevisiae*," *RSC Advances* 5 (2015): 79184.

20. M. Kitching, M. Ramani, and E. Marsili, "Fungal biosynthesis of gold nanoparticles: Mechanism and scale up," *Microbial Biotechnology* 8 (2015): 904–917.

21. A. Zielonka and M. Klimek-Ochab, "Fungal Synthesis of Size-Defined Nanoparticles," *Advance Nature Science: Nanoscience Nanotechnology* 8 (2017): 043001.

22. S. Parveen, S. N. Islam, and A. Ahmad, "Mycological synthesis of Ruthenium oxide quantum dots and their application in the colorimetric detection of H2O2," *Advanced Powder Technology* 33 (2022): 103861.

23. A. Sugunan, P. Melin, J. Schnürer, J. G. Hilborn, and J. Dutta, "Nutrition-Driven Assembly of Colloidal Nanoparticles: Growing Fungi Assemble Gold Nanoparticles as Microwires," *Advanced Materials* 19 (2007): 77–81.

24. H. Wang, X. Li, L. Chai, and L. Zhang, "Nano-functionalized filamentous fungus hyphae with fast reversible macroscopic assembly & disassembly features," *Chemical Communications* 51 (2015): 8524–8527.

25. Z. Li, S.-W. Chung, J.-M. Nam, D. S. Ginger, and C. A. Mirkin, "Living Templates for the Hierarchical Assembly of Gold Nanoparticles," *Angewandte Chemie International Edition* 42 (2003): 2306–2309.

26. R. F. Fakhrullin, A. I. Zamaleeva, M. V. Morozov, et al., "Living Fungi Cells Encapsulated in Polyelectrolyte Shells Doped with Metal Nanoparticles," *Langmuir* 25 (2009): 4628–4634.

27. A. M. Kubo, L. F. Gorup, L. S. Amaral, E. R. Filho, and E. R. Camargo, "Kinetic Control of Microtubule Morphology Obtained by Assembling Gold Nanoparticles on Living Fungal Biotemplates," *Bioconjugate Chemistry* 27 (2016): 2337–2345.

28. R. Penman, R. Kariuki, Z. L. Shaw, et al., "Gold nanoparticle adsorption alters the cell stiffness and cell wall bio-chemical landscape of Candida albicans fungal cells," *Journal of Colloid and Interface Science* 654 (2024): 390–404.

29. H. Chen, B. Schmidt, A. Gennett, et al., "Extrusion-Based Additive Manufacturing of Complex Three-Dimensional Ultra-Lightweight Materials Using the Basidiomycete *Fomes Fomentarius*," *Material Advances* 6 (2025): 5149–5158.

30. B. Schmidt, C. Freidank-Pohl, J. Zillessen, et al., "Mechanical, Physical and Thermal Properties of Composite Materials Produced With the Basidiomycete Fomes Fomentarius," *Fungal Biology and Biotechnology* 10 (2023): 22.

31. W. Sun, S. H. Strässle Zúñiga, V. Philippe, L. Rinaldi, and T. Abitbol, "Mycelium-Bound Composites From Agro-Industrial Waste for Broadband Acoustic Absorption," *Materials & Design* 250 (2025): 113591.

32. F. Poohphajai, A. Gubenšek, A. Černoša, et al., "Bioinspired Living Coating System for Wood Protection: Exploring Fungal Species on Wood Surfaces Coated with Biofinish during Its Service Life," *Coatings* 14 (2024): 430.

33. M. Zhang, J. Xue, R. Zhang, et al., "Mycelium Composite with Hierarchical Porous Structure for Thermal Management," *Small* 19 (2023): 2302827.

34. A. Sandak, "Engineered Living Materials for Sustainable and Resilient Architecture," *Nature Reviews Materials* 8 (2023): 357–359.

35. C. Wobill, Z. Zhang, P. Fischer, and P. A. Rühs, "Anisotropic Growth of Filamentous Fungi in Wood Hydrogel Composites Increases Mechanical Properties," *ACS Applied Bio Materials* 8 (2025): 5024–5031.

36. S. Gantenbein, E. Colucci, J. Käch, et al., "Three-Dimensional Printing of Mycelium Hydrogels Into Living Complex Materials," *Nature Materials* 22 (2023): 128–134.

37. S. C. Shen, N. A. Lee, W. J. Lockett, et al., "Robust Myco-Composites: A Biocomposite Platform for Versatile Hybrid-Living Materials," *Materials Horizons* 11 (2024): 1689–1703.

38. E. Soh, J. H. Teoh, B. Leong, T. Xing, and H. L. Ferrand, "3D Printing of Mycelium Engineered Living Materials Using a Waste-Based Ink and Non-Sterile Conditions," *Materials & Design* 236 (2023): 112481.

39. E. Elsacker, A. Søndergaard, A. Van Wylick, E. Peeters, and L. De Laet, "Growing living and multifunctional mycelium composites for large-scale formwork applications using robotic abrasive wire-cutting," *Construction and Building Materials* 283 (2021): 122732.

40. A. van't Padje, L. O. Galvez, M. Klein, et al., "Temporal Tracking of Quantum-Dot Apatite Across in Vitro Mycorrhizal Networks Shows How Host Demand can Influence Fungal Nutrient Transfer Strategies," *The ISME Journal* 15 (2021): 435–449.

41. A. Dinius, Z. J. Kozanecka, K. P. Hoffmann, and R. Krull, "Intensification of Bioprocesses with Filamentous Microorganisms," *Physical Sciences Reviews* 9 (2024): 777–823.

42. A. J. Tough, J. Pulham, and J. I. Prosser, "A Mathematical Model for the Growth of Mycelial Pellet Populations," *Biotechnology and Bioengineering* 46 (1995): 561–572.

43. Y. Q. Cui, R. G. J. M. van der Lans, and K. C. A. M. Luyben, "Effect of Agitation Intensities on Fungal Morphology of Submerged Fermentation," *Biotechnology and Bioengineering* 55 (1997): 715–726.

44. Y. Q. Cui, W. J. Okkerse, R. G. J. M. van der Lans, and K. C. A. M. Luyben, "Modeling and Measurements of Fungal Growth and Morphology in Submerged Fermentations," *Biotechnology and Bioengineering* 60 (1998): 216–229.

45. M. Papagianni, "Advances in Citric Acid Fermentation by Aspergillus Niger: Biochemical Aspects, Membrane Transport and Modeling," *Biotechnology Advances* 25 (2007): 244–263.

46. M. Papagianni, "Fungal Morphology and Metabolite Production in Submerged Mycelial Processes," *Biotechnology Advances* 22 (2004): 189–259.

47. S. White, M. McIntyre, D. R. Berry, and B. McNeil, "The Autolysis of Industrial Filamentous Fungi," *Critical Reviews in Biotechnology* 22 (2002): 1–14.

48. G. C. Paul, C. A. Kent, and C. R. Thomas, "Hyphal Vocuolation and Fragmentation in Penicillium Chrysogenum," *Biotechnology and Bioengineering* 44 (1994): 655–660.

49. T. Nomura, S. Tani, M. Yamamoto, et al., "Cytotoxicity and Colloidal Behavior of Polystyrene Latex Nanoparticles Toward Filamentous Fungi in Isotonic Solutions," *Chemosphere* 149 (2016): 84–90.

50. J. Ruiz-Herrera, "Biosynthesis of β-Glucans in Fungi," *Antonie Van Leeuwenhoek* 60 (1991): 73–81.

51. Z. Ma, M. Xu, Q. Wang, et al., "Development of an Efficient Strategy to Improve Extracellular Polysaccharide Production of Ganoderma lucidum Using L-Phenylalanine as an Enhancer," *Frontier Microbiology* 10 (2019): 2306.

52. V. Kachrimanidou, A. Papadaki, H. Papapostolou, M. Alexandri, Z. Gonou-Zagou, and N. Kopsahelis, "Ganoderma Lucidum Mycelia Mass and Bioactive Compounds Production Through Grape Pomace and Cheese Whey Valorization," *Molecules (Basel, Switzerland)* 28 (2023): 6331.

53. R. S. Cherry and E. T. Papoutsakis, "Hydrodynamic Effects on Cells in Agitated Tissue Culture Reactors," *Bioprocess Engineering* 1 (1986): 29–41.

54. J.-J. Oh, S. Ammu, V. D. Vriend, et al., "Growth, Distribution, and Photosynthesis of Chlamydomonas Reinhardtii in 3D Hydrogels," *Advanced Materials* 36 (2024): 2305505.

55. A. Armada-Moreira, A. M. Dar, Z. Zhao, et al., "Plant Electrophysiology With Conformable Organic Electronics: Deciphering the Propagation of Venus Flytrap Action Potentials," *Science Advances* 9 (2023): adh4443.

56. C. Zhao and F. Tombola, "Voltage-Gated Proton Channels From Fungi Highlight Role of Peripheral Regions in Channel Activation," *Communications Biology* 4 (2021): 1.

57. P. M. Kane, "Proton Transport and pH Control in Fungi," *Advances in Experimental Medicine and Biology* 892 (2016): 33.

58. R. R. Lew, "Mapping Fungal Ion Channel Locations," *Fungal Genetics and Biology* 24 (1998): 69–76.

59. A. K. Mishra, J. Kim, H. Baghdadi, B. R. Johnson, K. T. Hodge, and R. F. Shepherd, "Sensorimotor Control of Robots Mediated by Electrophysiological Measurements of Fungal Mycelia," *Science Robotics* 9 (2024): adk8019.

60. R. M. Jones, R. W. Reynolds, A. K. Thurston, and R. A. Barbato, "Fungal Tissue as a Medium for Electrical Signal Transmission: A Baseline Assessment With Melanized Fungus Curvularia Lunata," *IEEE Journal of Electromagnetics, RF and Microwaves in Medicine and Biology* 9 (2025): 206–213.

61. R. Mayne, N. Roberts, N. Phillips, R. Weerasekera, and A. Adamatzky, "Propagation of Electrical Signals by Fungi," *Bio Systems* 229 (2023): 104933.

62. G. Dufil, J. Pham, C. Diacci, et al., "Glucose-Sensitive Biohybrid Roots for Supercapacitive Bioanodes," *ACS Applied Bio Materials* 7 (2024): 8632–8641.

63. P. Welch, "The Use of Fast Fourier Transform for the Estimation of Power Spectra: A Method Based on Time Averaging Over Short, Modified Periodograms," *IEEE Transactions on Audio and Electroacoustics* 15 (1967): 70–73.

64. X. Yuan, H. Xu, X. Liu, et al., "Engineered Living Energy Materials," *Interdisciplinary Materials* 4 (2025): 412–455.

65. S. Sharma, S. K. Ammu, P. Thakolkaran, J. Jovanova, K. Masania, and S. Kumar, "Piezoelectric Truss Metamaterials: Data-Driven Design and Additive manufacturing," *npj Metamaterials* 1 (2025): 9.

66. S. K. Ammu, X. Chen, D. G. Ulcay, et al., "3D Printing of Lead-Free Piezoelectric Ultrasound Transducers," *Advanced Materials Technologies* 9 (2024): 2400858.

67. M. Amani, K. Weiland, M. Ablonczy, et al., "Enhancing the Ultrasonic Welding of Wood Using 3D Printed Lignin Energy Directors," *Advanced Science* 13, no. 15: 07055.

68. S. Patranabish, *Studies on the Nematic Phases of Flexible and Rigid Bent Core Liquid Crystals Extension to Polymers for Energy Harvesting Applications* (Department of Physics, 2022).

69. S. Oh, H. Jung, Y.-H. Kim, et al., "Characterization of ITO Etching by Spontaneously Evaporated Fume of Hydrogen Chloride," *Microelectronic Engineering* 103 (2013): 173–176.

70. S.-H. Su, H.-J. Kong, C.-L. Tseng, and G.-Y. Chen, "Wet Etching Mechanism and Crystallization of Indium–tin Oxide Layer for Application in Light-emitting Diodes," *Japanese Journal of Applied Physics* 57 (2017): 01AE05.

71. S. Schyck, M. Ablonczy, S. Patranabish, and K. Masania, "Data underlying the article: Shaping of Biohybrid Functional Living Materials [Data set] 4TU.ResearchData", (2026): https://doi.org/10.4121/688d5cbe-8438-4051-a6df-3723fd8ffb12.

Supporting Information

Additional supporting information can be found online in the Supporting Information section.

Supporting File: adfm74977-sup-0001-SuppMat.docx.